ANALYSIS ON THERMAL AND HYDRAULIC PERFORMANCE OF A T-SHAPED VAPOR CHAMBER DESIGNED FOR MOTORCYCLE LED LIGHTS

by

Qifei JIAN[a*], Cong LI[a], and Li WANG[b]

[a] School of Mechanical and Automotive Engineering, South China University of Technology, Guangzhou, Guangdong, China

[b] Haigang Jie, 234 Xing Gang East Road, Guangzhou, Guangdong, China

Original scientific paper
https://doi.org/10.2298/TSCI170411231Q

Experiment and numerical analyses were conducted to study the thermal performance and circulation characteristic of the working fluid of a T-shaped vapor chamber special designed for the motorcycle LED light. The influences of heat loads and cooling magnitude were experimentally investigated. Results show that both the heat loads and cooling conditions have strong influences on the thermal performance of the vapor chamber, and the thermal resistance in the extended section occupies over 75.8% of the overall thermal resistance of the vapor chamber. Simulation results indicate that large pressure drop occurs along the extended section of the vapor chamber, and causes large temperature difference along the extended section.

Key words: *vapor chamber, pressure drop, heat transfer, thermal resistance, numerical analysis, heat conduction*

Introduction

Vapor chamber (VC) has been an excellent candidate for solving the thermal management problems in many industries, such as electronic systems. The VC can swiftly spread heat from a hot spot to the surroundings. Studies of the influences of inner structure on the thermal performance of the VC have been conducted by many researchers. Li *et al.* [1] experimentally investigated the manufactured copper water VC with two wick structures. Their results showed that VC with copper foam wick structures exhibit good temperature uniformity and VC with copper powder exhibit low thermal resistance. A study conducted by Reyes *et al.* [2] was proposed on the behavior of a vertically placed VC based heat spreader intended for avionics applications. A mini-evaporator area made up of an array of mini-fin-pins was implemented for enhancing the boiling inside the VC. The experiment results showed that from the heat transfer standpoint, VC heat spreaders were always more efficient. Other studies focus on the effect of the wick structures could be seen in [3-10]. The vapor space height, evaporator section structure and the fill ratio of working fluid have also been considered in other studies. Huang *et al.* [11] fabricated and tested the VC with five different vapor space heights. They found that the VC achieved the optimum design when the hydraulic diameter ratio was greater than 0.6. Tsai *et al.* [12] experimentally investigated the influence of heating power, fill ratio of working fluid, and evaporator surface structure on the thermal performance of a two-phase VC system for

* Corresponding author, e-mail: melicong0719@mail.scut.edu.cn; tcjqf@scut.edu.cn

electronic cooling. The results suggested that either a growing heating power or a decreasing fill ratio decreased the overall thermal resistance, and the surface influenced the evaporator function prominently.

Numerical analysis is an effective method for analyzing the hydrothermal characteristics of the VC. In the study of Zuo and Faghri [13], the vapor core was treated as a single interface between the evaporator and condenser so as to avoid dealing with the two-phase problem, and only the heat conduction between each control volume is considered. Similar method is also seen in the studies of Chen *et al.* [14] and [15], and Lu *et al.* [16]. Their method, [13-16], is very easy to use, very time efficient and agrees well with the experiment results. In the work of Vadakkan *et al.* [17], a 3-D model to analyze the transient and steady-state performance of flat heat pipes subjected to heating with discrete heat sources is proposed. Vapor flow, temperature and hydrodynamic pressure fields are computed from coupled continuity/momentum and energy equations in the wick and vapor regions. Their analysis highlights the importance of considering axial diffusion through the wall and wick in determining the temperature distribution in flat heat pipes.

Above all, the influences of VC inner structures on thermal performance of VC have been studied by many researchers. Since the outer shape of VC must fit the components that need heat dissipation, the outer shape thus may also influence the heat transfer performance of VC. However, previous studies rarely considered the influences of the outer shape of VC. In this paper, the thermal performance of a T-shaped VC (TSVC) special designed for the thermal management of motorcycle high power LED lights was studied experimentally. The influences of heat loads and cooling capability of heat sink were considered. Numerical model has also been proposed based on FLUENT [16, 18, 19], to investigate the thermal hydrodynamic characteristics of the working fluid inside the TSVC. The results obtained in this paper could provide references on improving the thermal performance of this TSVC.

Thermal performance test

Thermal performance apparatus is shown in fig. 1. The apparatus for thermal performance test were established for studying the thermal performance of this TSVC. The photograph of the TSVC is shown in fig. 2. Figure 2(b) shows the operating mechanism of the TSVC. The TSVC is made of copper and de-ionized water is used as the working fluid.

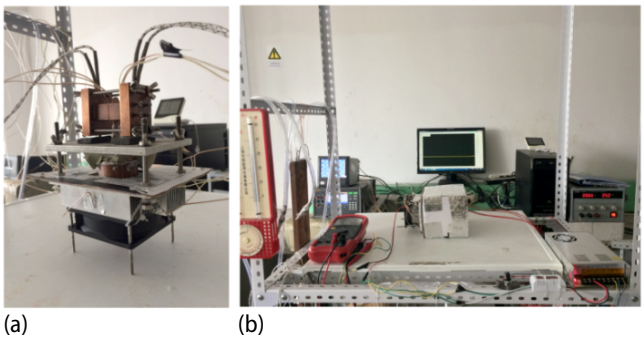

Figure 1. Experiment apparatus for testing the TSVC

In the thermal performance test, two rod heaters embedded in the copper heating blocks, as shown in fig. 3(a), were used as the heating sources. Heat was transferred through the heat conduction blocks to the evaporation section of the TSVC. Thermal silicone grease was applied between the heat conduction block and the TSVC evaporation section to remove the air-gap. Thermal conductivity of the thermal silicone grease is 2.0 W/mK. Heating power of the rod heaters were varied by DC power supply (ATTEN TPR3020S). The voltage applied on the rod heater was ranging from 5 V to 14 V in 3 V increments. As shown in fig. 3, the evaporation section was located at both sides of the extended section. The heating

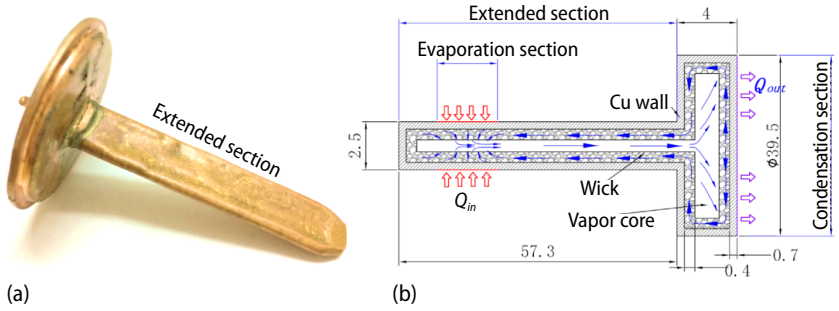

Figure 2. Schematic diagram of the TSVC

area was $12.5\ \text{mm} \times 15\ \text{mm}$ on each side of the extend section. The condensation section was cooled by the heat sink with air fan. The fan speed was controlled by voltage regulator and DC converter to vary the cooling air-flow rate. The voltage applied on the fan was increased from 5 V to 17 V in 3 V increments. The ambient temperature is about $298 \pm 1.5\text{K}$. The 19 OMEGA K-type thermocouples (defined as $T_1 \sim T_{19}$) and FLUKE 2638A digital data logger were used to measure the temperature at different positions. Detailed location of thermocouples was also illustrated in fig. 3.

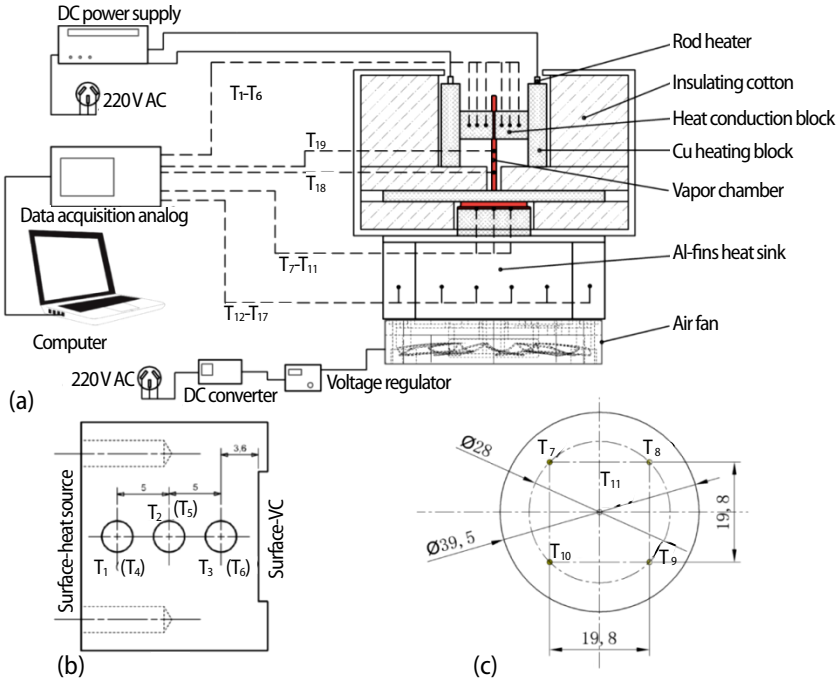

Figure 3. Schematic diagram of the thermal performance of TSVC

Based on energy conservation and Fourier heat conduction law, the temperature of evaporation section of TSVC contacted with the heat conduction block is calculated and expressed:

$$T_h = 0.5\left\{\left[T_3 - \frac{h_{3-h}}{h_{2-h}}(T_2 - T_3)\right] + \left[T_2 - \frac{h_{2-h}}{h_{1-2}}(T_1 - T_2)\right]\right\} \tag{1}$$

In eq. (1), h_{i-j} is the length between the measurement point i and j, $i = 1,2,3$; $j = 2,\mathrm{h}$. The subscript h refers to the surface between the copper heating block and VC, as shown in fig. 3. The temperature of condensation section surface of the VC is set as the average temperature of the five thermal couples located at the interface between the heat sink and VC, and is calculated:

$$T_c = 0.2(T_7 + T_8 + T_9 + T_{10} + T_{11}) \tag{2}$$

The overall thermal resistance, R_{VC}, of TSVC is determined using the expression as follows.

$$R_{\mathrm{VC}} = \frac{T_h - T_c}{Q} \tag{3}$$

Equivalent heat transfer coefficient of the heat sink, k_c, is calculated based on the temperature difference between the temperature of the condensation section surface of VC and the ambient.

$$k_c = \frac{Q}{A_c(T_c - T_\infty)} \tag{4}$$

Uncertainty analysis

The measurement error of the temperature data logger is 0.6K as presented in the manufacturer instructions, while the measurement error of the thermal couples is 0.2K. Assume that the uncertainties of data obey uniform distribution, the coverage factor K is $3^{1/2}$. Then the uncertainties of the temperature data acquisition instrument and the thermal couples are 0.346K, 0.1155K, respectively. According to the manufacturer instruction of DC power supply, the measurement errors of current and voltage are 0.5%rdg + 0.02 A and 0.5%rdg + 0.2 V, respectively.

The uncertainty of the temperature data directly measured by FLUKE 2638A digital data logger using thermal couples is 0.365K. Uncertainties of the current and voltage applied on the rod heaters are listed in tab. 1. The maximum uncertainty of the heating power applied on the evaporation section is 1.5095 W. Uncertainty of the overall thermal resistance of the TSVC is shown in fig. 4. The maximum uncertainty of the overall thermal resistance is 0.35 K/W as the heat load of 3.3 W and fan voltage of 17 V.

Table 1. Uncertainties of the current, voltage, and power applied on the rod heaters

Current [A]	Error [A]	Uncertainty [A]	Voltage [V]	Error [V]	Uncertainty [V]	Power [W]	Uncertainty [W]
0.66	0.0233	0.01345	5	0.225	0.1299	3.30	0.6359
1.06	0.0253	0.01461	8	0.240	0.1386	8.48	1.0605
1.44	0.0272	0.01570	11	0.255	0.1472	15.84	1.5095

Physical model

A 2-D physical model was developed to investigate the thermal hydrodynamic characteristics of the working fluid inside the VC. As shown in fig. 2(b), the TSVC was divided into

three sections, including extended section, evaporation section and condensation section. Sintered copper powder layer forms the wick structure of this VC. The copper powder has a diameter of about 141 μm. Heat load is applied on the evaporation section, which is 15 mm long in 2-D model. The condensation section has a diameter of 39.5 mm. Except the evaporation section and condensation section, all other outer walls are assumed adiabatic. For simplifying the model, the heat sink of the VC is equivalent to a convective heat transfer coefficient applied on the condensation section, and the equivalent convective heat transfer coefficient is calculated based on eq. (4). Thicknesses of copper wall and wick structure are 0.7 mm and 0.4 mm, respectively. The thermophysical properties of the copper wall and wick are given in tab. 2. The effective thermal conductivity of the wick structure is determined based on Maxwell's equation [20], expressed in eq. (5). The boundary conditions are determined according to the experiment set-up. The initial temperature all through the VC and ambient temperature are set as 298 K.

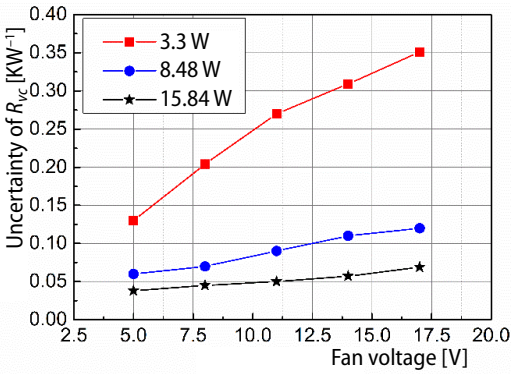

Figure 4. Uncertainty of the overall thermal resistance of TSVC *vs.* fan voltage

$$k_{\text{wick}} = k_{\text{wall}} \frac{2 + \dfrac{k_l}{k_{\text{wall}}} - 2\varepsilon\left(1 - \dfrac{k_l}{k_{\text{wall}}}\right)}{2 + \dfrac{k_l}{k_{\text{wall}}} + \varepsilon\left(1 - \dfrac{k_l}{k_{\text{wall}}}\right)} \tag{5}$$

Table 2. Thermophysical properties of the VC material and working fluid

Copper	Thermal conductivity	387.6 W/mK
	Specific heat	381 J/kgK
	Density	8978 kg/m^3
Wick	Thermal conductivity	104.874 W/mK
	Porosity	0.644
	Permeability	$2.67 \cdot 10^{-11}$ m^2
Water	Thermal conductivity	0.6 W/mK
	Specific heat	4182 J/kgK
	Density	984.645 kg/m^3
	Viscosity	0.000493 Ns/m^2
Water vapor	Thermal conductivity	0.0261 W/mK
	Specific heat	2014 J/kgK
	Density	0.116 kg/m^3
	Viscosity	$1.34 \cdot 10^{-5}$ Ns/m^2
Water/vapor	Latent heat of vaporization	2364.89 kJ/kg

Mathematical model and governing equations

According to the FHP network model proposed by Zuo and Faghri [13], the liquid return process in the wick is extremely important to the working fluid circulation, while it has

little effect on the heat transfer, thus neglecting the liquid-vapor interfacial convective heat exchange, and assuming that evaporation and condensation of the working fluid take place smoothly at the wick-vapor interface. As stated in the network model of Zuo and Faghri [13], the vapor flow thermal resistance is considerably smaller than the other processes inside the heat pipe, thus the vapor core is treated as a constant temperature interface. Other assumptions are listed as followings, as also stated in [21].

– A steady-state condition is established.
– Laminar flow in both the vapor core and wick section.
– The wick structure is isotropic and fully saturated.
– The gravity influence is negligible.

Similar assumptions could also be found in [15, 16] and the validity was confirmed. The energy balance at the interface is then obtained based on the energy conservation and Fourier heat conduction law, as shown in eq. (6). The users-define functions (UDF) were used to define the boundary conditions and source terms:

$$Q_e = \sum_i^{e-\text{wick}} \left[\frac{k_i A_i}{\frac{\Delta L}{2}} \left(T_i - T_v \right) \right] = Q_c = \sum_i^{c-\text{wick}} \left[\frac{k_i A_i}{\frac{\Delta L}{2}} \left(T_v - T_i \right) \right] \tag{6}$$

Thus, the vapor core temperature is then determined:

$$T_v = \frac{\sum_i \frac{k_i A_i}{\Delta L} T}{\sum_i \frac{k_i A_i}{\Delta L}} \tag{7}$$

The T_i is the interface temperature and ΔL represents the length of each grid cell. The subscript i represents the wick-vapor interface. The vapor core temperature, T_v, is determined using the UDF. Ignoring the liquid flow in tangential direction [17], then the mass conservation at each face of the liquid-vapor interface is determined:

$$m_i = \frac{\left[k_i A_i \left(T_i - T_v \right) \right]_{e-\text{wick}}}{h_{fg} \frac{\Delta L}{2}} = \frac{\left[k_i A_i \left(T_v - T_i \right) \right]_{c-\text{wick}}}{h_{fg} \frac{\Delta L}{2}} \tag{8}$$

$$V_{\text{normal},l} = \frac{m_i}{\rho_l A_l}, \quad V_{\text{normal},v} = \frac{m_i}{\rho_v A_v} \tag{9}$$

The continuity, momentum equations for wick region and vapor core and energy equation for the solid wall and wick region, and the vapor core are list:

$$\varepsilon \frac{\partial \rho}{\partial t} + \nabla (\rho \vec{\mathrm{V}}) = 0 \tag{10}$$

$$\rho \vec{\mathrm{V}} \nabla \vec{\mathrm{V}} = -\varepsilon \nabla p + \mu \nabla^2 \vec{\mathrm{V}} + S_D \tag{11}$$

$$\nabla^2 T = 0 \tag{12}$$

Details boundary conditions are listed in tab. 3. The UDF is used to calculate the local mass flux at each grid face of the interface based on eq. (5). The normal velocity at each face of

the interface is then obtained in eq. (6), and stored as a boundary file. The SIMPLE algorithm and control volume method are employed to solve the governing equations using FLUENT 6.3. Convergence of the energy equation is estimated as relative error between the heat input at evaporator wall and the heat output at condenser wall is within $\pm 0.05\%$.

Table 3. Boundary conditions of the numerical model

Wick-vapor interface	$\rho_l \overrightarrow{V_l} = \rho_v \overrightarrow{V_v}$ $T = T_v = T_{sat}$
Evaporation section	$k_{wall}(\partial T/\partial y) = q$
Condensation section	$-k_{wall}(\partial T/\partial y) = k_c(T_c - T_\infty)$
Adiabatic walls	$k_{wall}(\partial T/\partial y) = 0$
Solid wall-wick region interface	$k_{wall}(\partial T_{wall}/\partial n) = k_{wick}(\partial T_{wick}/\partial n)$ $v = u = 0$

Mesh independence and numerical model validation

Before the simulation analysis, mesh independence needed to be demonstrated by comparing the results in different mesh numbers. Five mesh numbers (22060, 26696, 29482, 40200, and 58714) were tested and compared. The heat flux was set as 2000 W/m^2 on each side of the evaporation section. The equivalent convective heat transfer coefficient at the condensation section and the ambient temperature were set as 200 W/m^{2}K and 298 K, respectively. Based on the comparisons results, the mesh number of 40200 was selected for numerical calculation.

In order to validate the numerical model, the simulation results were compared with the experiment conducted in this paper. Figure 5 shows the comparisons of the evaporation section temperature of the numerical results and experiment results in this paper. It can be seen the maximum relative error of the simulation result with the experiment results in this paper is less than 1%. Therefore, the simplified numerical model proposed in this paper could be considered reliable.

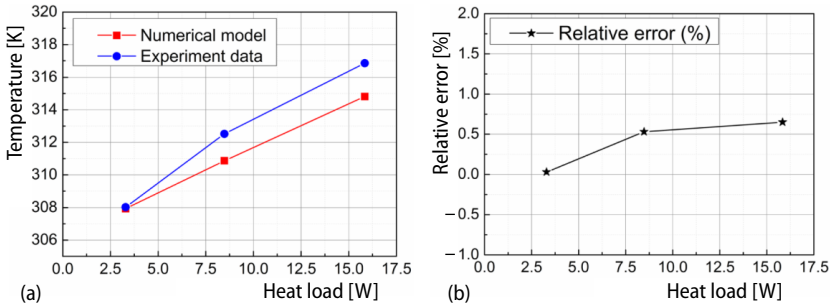

Figure 5. Model validation with the experiment results in this paper

Results and discussion

Figure 6 shows the velocity and pressure distribution of the TSVC as the heat load is 15.84 W, and the cooling fan voltage is 11 V. The circulation of the working fluid inside the TSVC is shown in fig. 6(a). Figure 6(c) illustrates the pressure variation inside the vapor core. The A-B section refers to the evaporation section, while D-E section refers to the bottom space between the outlet of extended section and condensation section. Pressure drop along the extended section is considered to include two parts (Δp_{A-B} and Δp_{B-D}). The pressure drop Δp_{A-B} represents the pressure loss of the fluid at the evaporation section, while Δp_{B-D} is the pressure drop vapor flowing along the extended section.

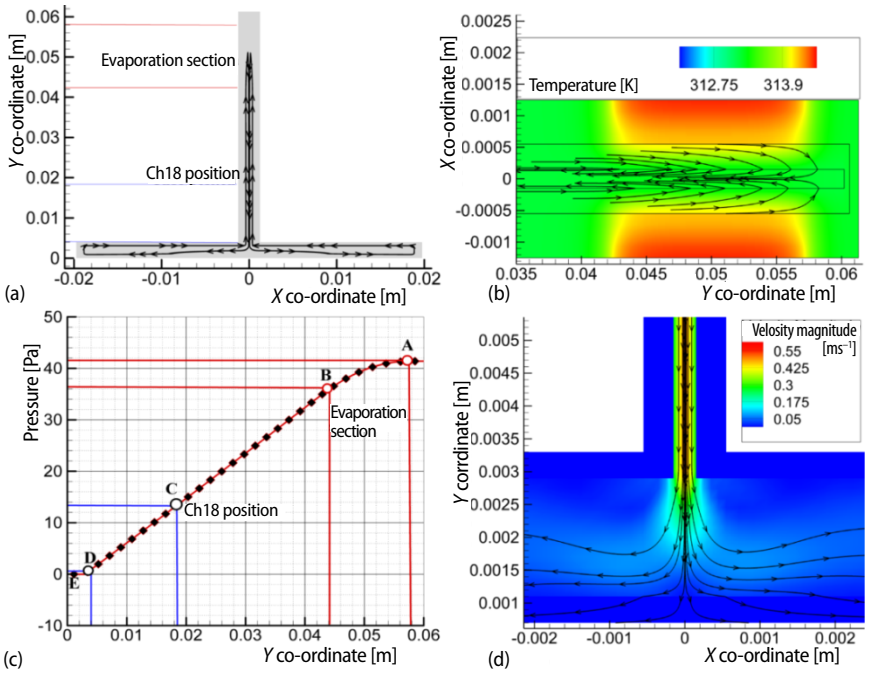

Figure 6. Velocity distribution of the working fluid in the TSVC; (a) circulation of the fluid in TSVC, (b) fluid velocity distribution at evaporation section, (c) pressure variation in vapor core, (d) fluid velocity distribution at condensation section

Because of the symmetrically located heat sources, the vapor flows into the vapor core in opposite direction at the evaporation section, shown in fig. 6(b). The opposite direction flow could cause large pressure loss, represented by Δp_{A-B}. The second part of pressure loss Δp_{B-D} is caused by the effect of shear stress at the wick-vapor interface along the extended section and high vapor velocity. When the vapor velocity is sufficient to entrain liquid returning to the evaporation section, the thermal performance and evaporation in the evaporator will decline. And the shear stress at the wick-vapor interface could hinder the flow of working fluid flowing to the evaporation section, worsen the evaporation progress in the wick and cause dry-out situation. Figure 6(c) indicates that the pressure drop between the evaporation section and Ch18 location (represented by Δp_{A-D}) is much larger than that between the location of Ch18 and the condensation section (represented by Δp_{D-E}).

The Ch18 and Ch19 (corresponding to T_{18} and T_{19}) were the data acquisition channels of two thermal couples located at the extended section, as shown in fig. 3. The overall thermal resistance of the TSVC is considered to be divided into two parts: the thermal resistance between the evaporation section and Ch18, and the thermal resistance between Ch18 and the condensation section.

$$R_{Th-Tch18} = \frac{T_h - T_{Ch18}}{Q} \tag{13}$$

$$R_{Tc-Tch18} = \frac{T_{Ch18} - T_c}{Q} \tag{14}$$

Variation of the ratio $R_{Th-Tch18}/R_{VC}$ and $R_{Tc-Tch18}/R_{VC}$ *vs.* heat loads and fan voltages is shown in fig. 7. The thermal resistances $R_{Th-Tch18}$ and $R_{Tc-Tch18}$ are defined and expressed in eqs. (13) and (14). The $R_{Th-Tch18}$ is the thermal resistance between the evaporation section of the TSVC and the location of Ch18, while $R_{Tc-Tch18}$ is the thermal resistance between the condensation section of the TSVC and the location of Ch18. It can be observed from fig. 7 that the thermal resistance ($R_{Th-Tch18}$) between the evaporation section and Ch18 occupies more than 60% of the overall thermal resistance, R_{VC}. And the proportion of $R_{Th-Tch18}$ increases with the increase of heat loads. When the heat load is 15.84 W, the proportion of $R_{Th-Tch18}$ is in the range of 75.8% ~ 92.4% for different cooling fan voltages, while $R_{Tc-Tch18}$ takes over only 7.59% ~ 24.18%. The extended section of the TSVC is considered to contribute the main thermal resistance proportion to the overall thermal resistance of the TSVC.

$$\frac{\Delta \ln P}{\Delta T} = \frac{h_{fg}}{R_{gas} T^2}$$

Since the thermal resistance could be represented by temperature difference, and according to the Clausius-Clapeyron equation, eq. (15), the large pressure drop could result in large temperature differences, similar results could also be seen in fig. 6. Since Δp_{A-C} is higher than Δp_{C-E} as shown in fig. 6(c), the temperature difference $\Delta T_{Th-Tch18}$ is then larger than $\Delta T_{Tc-Tch18}$ based on the Clausius-Clapeyron equation. The Δp_{D-E} is the pressure drop from the outlet of the extended section to the condensation section, and is much small as compared to Δp_{A-D}, as shown in fig. 6(c), which causes much smaller temperature difference than in the extended section.

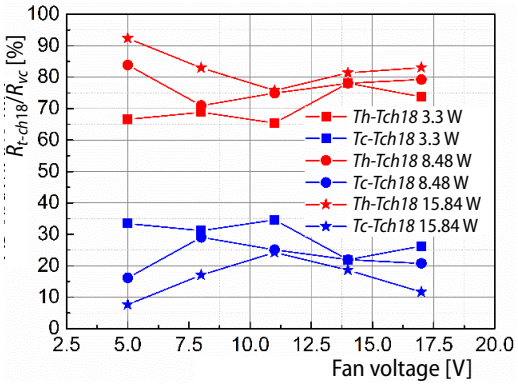

Figure 7. Variation of ratio $R_{Th-Tch18}/R_{VC}$ and $R_{Tc-Tch18}/R_{VC}$ with different heat loads and fan voltages

The thermal performance of the TSVC was experimentally investigated by applying various heat loads and cooling conditions (varied by the fan voltages). Temperature difference between the evaporation section and condensation section is shown in fig. 8(a). It can be seen that the temperature difference increases with the increase of cooling fan voltage and heat load. When the voltage applied on the rod heaters is 11 V, the heat load reaches 15.84 W, and with the fan voltage of 5 V, the temperature difference between the evaporation and condensation section of the TSVC is 6.35 K. However, as the fan voltage is 17 V, the temperature difference reaches 11.44 K.

Variation of the overall thermal resistance, R_{VC}, of the TSVC *vs.* heat loads and cooling fan voltages are illustrated in fig. 8(b). The overall thermal resistance of this TSVC increases with the increase of cooling fan voltages. However, as the heat loads increases, the overall thermal resistance decreases. When the voltage applied on the rod heaters is 5 V, the heat load is 3.3 W, and the overall thermal resistance of the TSVC is ranging from 0.679 K/W ~ 1.826 K/W, which is much higher than in the other two heat loads conditions. The overall thermal resistance reaches the minimum value in all these three heat loads conditions when then cooling fan voltage is 5 V. The minimum thermal resistances of the TSVC

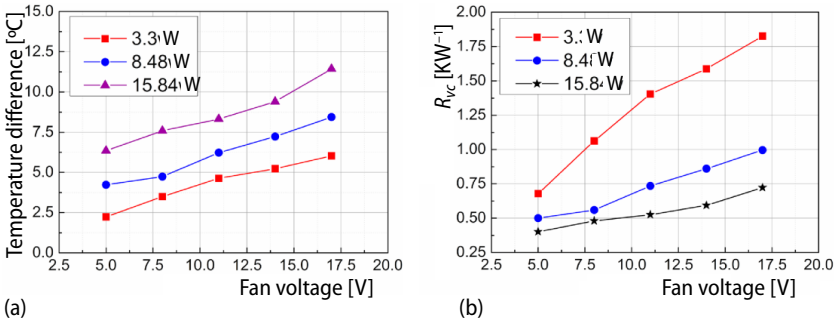

Figure 8. Temperature difference between the evaporation condensation section (a) and variation of the overall thermal resistance of TSVC (b) *vs.* different heat loads and fan voltages

corresponding to the heat load of 3.3 W, 8.48 W and 15.84 W are 0.679 K/W, 0.499 K/W, and 0.401 K/W, respectively.

Conclusions

Both experiment and numerical analysis were conducted to investigate the heat transfer performance of a TSVC designed for the thermal management of motorcycle high power LED lights. The influences of heat loads and cooling conditions on the thermal performance of the TSVC were investigated experimentally. Results indicate that both the heat loads and cooling magnitude have strong influences on the thermal performance of the TSVC, and the thermal resistance in the extended section occupies most proportion of the overall thermal resistance of the TSVC. When the heat load is 15.84 W, the proportion of $R_{Th-Tch18}$ in the overall thermal resistance of the TSVC is in the range of 75.8% ~ 92.4% for different cooling fan voltages, while $R_{Tc-Tch18}$ takes over only 7.59% ~ 24.18%.

Experiment results also suggest that the overall thermal resistance of the TSVC increases with the increase of heat loads and cooling fan voltage. The minimum thermal resistances of the TSVC are 0.679 K/W, 0.499 K/W , and 0.401 K/W corresponding to the heat loads of 3.3 W, 8.48 W, and 15.84 W and the cooling fan voltage is 5 V, respectively. The proposed numerical model was validated by comparing with the experiment results. The circulation characteristic of working fluid inside this TSVC was obtained according to the simulation results. The results indicate that large pressure drop occurs along the extended section of the TSVC, which causes large temperature difference. Thus the design of the extended section of this TSVC plays an important role in enhancing the thermal performance of this TSVC.

Acknowledgment

This research was supported by the National Natural Science Foundation of China (21776095), the Guangzhou Science and Technology Program (No. 201804020048).

Nomenclature

A – area, [m^2]
h – distance, [m]
h_{fg} – latent heat of vaporization, [kJkg^{-1}]
k – thermal conductivity, [Wm^{-1}K^{-1}]
k_c – convective heat transfer coefficient, [Wm^{-2}K^{-1}]
ΔL – side length of a control volume, [m]
m_i – mass flux, [kgs^{-1}]
p – pressure, [Pa]

Q – heat transfer rate, [W]
q – heat flux, [Wm^{-2}]
R – thermal resistance, [KW^{-1}]
R_{gas} – gas constant
T – temperature, [K]
$\vec{V}$ – velocity vector, [ms^{-1}]

Greek symbols

ε – wick porosity
ρ – density, [kgm^{-3}]

Subscript

c – condensation section
e – evaporation section
i – wick-vapor interface
l – liquid region
normal, l – normal direction in liquid interface
normal, v – normal direction in vapor interface
sat – saturation
v – vapor region
wall – solid wall
wick – wick structure
∞ – ambient

References

[1] Li, Y., *et al.*, Experimental Investigation of Vapor Chambers with Different Wick Structures at Various Parameters, *Experimental Thermal and Fluid Science, 77* (2016), Oct., pp. 132-143
[2] Reyes, M., *et al.*, Experimental and Theoretical Study of a Vapour Chamber Based Heat Spreader for Avionics Applications, *Applied Thermal Engineering, 37* (2012), May, pp. 51-59
[3] Mengyao, W., *et al.*, Experimental Characterization of Si Micropillar Based Evaporator for Advanced Vapor Chambers, *Proceedings,* IEEE 16th Electronics Packaging Technology Conference (EPTC), Singapore, 2014, pp. 335-340
[4] Peng, Y., *et al.*, A Novel Wick Structure of Vapor Chamber Based on the Fractal Architecture of Leaf Vein, *International Journal of Heat and Mass Transfer, 63* (2013), Aug., pp. 120-133
[5] Zhen, S., Huihe, Q., An Asymmetrical Vapor Chamber with Multiscale Micro/Nanostructured Surfaces, *International Communications in Heat and Mass Transfer, 58* (2014), Nov., pp. 40-44
[6] Sprinceana, S., *et al.*, Capillary Layer Structure Effect upon Heat Transfer in Flat Heat Pipes, *Proceedings,* 7th International Conference on Advanced Topics in Optoelectronics, Microelectronics, and Nanotechnologies (ATOM-N), Vol. 9258, Constanta, Romania, 2014
[7] Ji, X., *et al.*, A Vapor Chamber Using Extended Condenser Concept for Ultra-High Heat Flux and Large Heater Area, *International Journal of Heat and Mass Transfer, 55* (2012), 17-18, pp. 4908-4913
[8] Weibel, J. A., *et al.*, Design of Integrated Nanostructured Wicks for High-Performance Vapor Chambers, *IEEE Transactions on Components Packaging and Manufacturing Technology, 1* (2011), 6, pp. 859-867
[9] Weibel, J. A., *et al.*, Experimental Characterization of Capillary-Fed Carbon Nanotube Vapor Chamber Wicks, *Journal of Heat Transfer-Transactions of the Asme, 135* (2013), 2, 021501
[10] Ju, Y. S., *et al.*, Planar Vapor Chamber with Hybrid Evaporator Wicks for the Thermal Management of High-Heat-Flux and High-Power Optoelectronic Devices, *International Journal of Heat and Mass Transfer, 60* (2013), May, pp. 163-169
[11] Huang, C. K., *et al.*, The Effects of Vapor Space Height on the Vapor Chamber Performance, *Experimental Heat Transfer, 25* (2012), 1, pp. 1-11
[12] Tsai, T.-E., *et al.*, Two-Phase Closed Thermosyphon Vapor-Chamber System for Electronic Cooling, *International Communications in Heat and Mass Transfer, 37* (2010), 5, pp. 484-489
[13] Zuo, Z. J., Faghri, A., A Network Thermodynamic Analysis of the Heat Pipe, *International Journal of Heat and Mass Transfer, 41* (1998), 11, pp. 1473-1484
[14] Chen, Y.-S., *et al.*, Numerical Simulation of a Heat Sink Embedded with a Vapor Chamber and Calculation of Effective Thermal Conductivity of a Vapor Chamber, *Applied Thermal Engineering, 29* (2009), 13, pp. 2655-2664
[15] Chen, Y.-S., *et al.*, A Simplified Transient Three-Dimensional Model for Estimating the Thermal Performance of the Vapor Chambers, *Applied Thermal Engineering, 26* (2006), 17-18, pp. 2087-2094
[16] Lu, L., *et al.*, Numerical Analysis on Thermal Hydraulic Performance of a Flat Plate Heat Pipe with Wick Column, *Heat and Mass Transfer, 51* (2015), 8, pp. 1051-1059
[17] Vadakkan, U., *et al.*, Transport in Flat Heat Pipes at High Heat Fluxes from Multiple Discrete Sources, *Journal of Heat Transfer-Transactions of the ASME, 126* (2004), 3, pp. 347-354
[18] Karabulut, K., *et al.*, Numerical Investigation of the Effect of Insulation on Heat Transfer of Thermal Bridges with Different Types, *Thermal Science, 20* (2016), 1, pp. 185-195
[19] Arslan, K., Three-Dimensional Computational Fluid Dynamics Modeling of TiO_2/R134a Nanorefrigerant, *Thermal Science, 21* (2017), 1A, 175-186

[20] M. J. C., *A Treatise on Electricity and Magnetism*, Clarendon Press, Oxford, UK, 1954
[21] Koito, Y., *et al.*, Fundamental Experiments and Numerical Analyses on Heat Transfer Characteristics of a Vapor Chamber - (Effect of Heat Source Size), *JSME International Journal Series B-Fluids and Thermal Engineering, 49* (2006), 4, pp. 1233-1240

Paper submitted: April 11, 2017
Paper revised: November 8, 2017
Paper accepted: November 9, 2017